Heliyon 10 (2024) e24964

Contents lists available at ScienceDirect

Heliyon

journal homepage: www.cell.com/heliyon

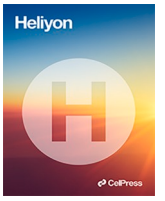

Research article

Improved liquid phase exfoliation technique for the fabrication of MoS_2/graphene heterostructure-based photodetector

B.J. Akeredolu [a,b,c,*], I. Ahemen [a], A.N. Amah [a], A.D. Onojah [a], Jyoti Shakya [c], H. N. Gayathri [c], Arindam Ghosh [c,d]

[a] Department of Physics Joseph Sarwuan Tarka University, Makurdi, P.M.B. 2373, Nigeria
[b] Department of Pure and Applied Physics Federal University, Wukari, P.M.B 1020, Nigeria
[c] Department of Physics, Indian Institute of Science, Bangalore, 560012, India
[d] Centre for Nano Science and Engineering, Indian Institute of Science, Bangalore, 560012, India

ARTICLE INFO

Keywords:
Molybdenum disulphide
Graphene
Photodetectors
Nanostructure
Exfoliation

ABSTRACT

2D nanosheets produced using liquid phase exfoliation method offers scalable and cost effective routes to optoelectronics devices. But this technique sometimes yields high defect, low stability, and compromised electronic properties. In this work, we employed an innovative approach that improved the existing liquid phase exfoliation method for fabricating MoS_2/graphene heterostructure-based photodetector with enhanced optoelectronic properties. This technique involves hydrothermally treating MoS_2 before dispersing it in a carefully chosen and environmentally friendly IPA/water solvent for ultrasonication exfoliation through an optomechanical approach. Thereafter, heterostructure nanosheets of MoS_2 and graphene were formed through sequential deposition technique for the fabrication of vertical heterojunctions. Furthermore, we achieved a vertically stacked MoS_2/graphene photodetector and a bare MoS_2 photodetector. The MoS_2/graphene hybrid nanosheets were characterized using spectroscopic and microscopic techniques. The results obtained show the size of the nanosheets is between 350 and 500 nm on average, and their thickness is less than or equal to 5 nm, and high crystallinity in the 2H semiconducting phase. The photocurrent, photoresponsivity, external quantum efficiency (EQE), and specific detectivity of MoS_2/graphene heterostructure at 4 V bias voltage and 650 nm illumination wavelength were 3.55 μA, 39.44 mA/W, 7.54 %, and 2.02×10^{10} Jones, respectively, and that of MoS_2 photodetector are 0.55 μA, 6.11 mA/W, 1.16 %, and 3.4×10^9 Jones. The results presented indicate that the photoresponse performances of the as-prepared MoS_2/graphene were greatly improved (about 7-fold) compared to the photoresponse of the sole MoS_2. Again, the MoS_2/graphene heterostructure fabricated in this work show better optoelectronic characteristics as compared to the similar heterostructure prepared using the conventional solution processed method. The results provide a modest, inexpensive, and efficient method to fabricate heterojunctions with improved optoelectronic performance.

1. Introduction

The recent curiosity of researchers in two-dimensional, 2D systems is largely due to their exceptional electrical, optical, and

* Corresponding author. Department of Pure and Applied Physics Federal University, Wukari, P.M.B. 1020, Nigeria.
E-mail address: akeredolu@fuwukari.edu.ng (B.J. Akeredolu).

https://doi.org/10.1016/j.heliyon.2024.e24964
Received 17 September 2023; Received in revised form 11 January 2024; Accepted 17 January 2024
Available online 26 January 2024

mechanical properties [1–4] that depend on the layer thickness and crystalline size [5]. Examples of this materials include; graphene, silicene [6], boron nitride (hexagonal) [7], phosphorene, transition-metal dichalcogenides (TMDs: MoS_2, $MoSe_2$ WS_2, etc.) [8], metal (basic) oxides (e.g., MoO_3) [9], metal halides (e.g., $MgBr_2$) [10], etc. Among the various layered materials apart from graphene, TMDs have gained considerable research focus for their excellent performances in optoelectronics and electronics applications. Molybdenum disulphide (MoS_2) is a typical TMD that is widely known to be a promising optoelectronic material [11]. Its structure comprises of an ultrathin layer of molybdenum enclosed between two sulphur atoms layers which are coupled together by van der Waals forces [12, 13]. The properties of a single-layered MoS_2 and few-layered MoS_2 are distinct from bulk MoS_2 [13,14]. In MoS_2, the bulk form with a band gap value of 1.3 eV is an indirect transition type, while the single-layered form has a direct band gap of approximately 1.8 eV [13, 15]. This allows for modification of the material's band structure. Also, the few-layered MoS_2 shows a significant direct transition, providing unique electronic [16], optical and catalytic properties [17], and a high carrier mobility along the in-plane direction [16, 18].

The heterostructure of graphene and MoS_2 have shown better performance in their constituent electronic properties combination. The hybrid heterostructure presents an opportunity to design and fabricate devices with different functions and stability in sundry fields, including electronics, biomedicine, energy storage, and optoelectronics [19–21]. Ultrafast application of photodetectors made of graphene with high carrier mobility is highly appealing. However, they suffer from weak absorption (2.3 %) and short carrier recombination lifetime in picosecond [22,23]. The combination of graphene and MoS_2 forms a hybrid photodetector with excellent photoresponsivity due to its high coefficient of absorption and large surface-to-volume ratio [24]. Numerous photodetectors based on 2D materials have been fabricated using various advance techniques such as advanced lithography method [25], van der Waal contact technique [26], and vertical Junction technique. Hu et al., 2023 used Asymmetric porous GaN/Graphene vertical junction to fabricate highly sensitive photodectector [27]. The van der Waal contact technique was used by Guo *et a.l* 2022 for self-powered photodetectors [26] etc. Other techniques used for synthesizing layered materials, include; mechanical cleavage, megasonic exfoliation [28], liquid phase exfoliation (LPE) [29], arc discharge [30], hydrothermal [31,32], and chemical vapour deposition (CVD) [33]. However, the LPE technique offers many advantages over other methods of synthesis; these include cost-effectiveness, simplicity, scalability, and compatibility with any substrate [34–36]. The LPE method can be carried out using one of three approaches: ultrasonication, shearing, or electrochemical [35,37]. To ensure a defect-free nanosheets synthesis from ultasonication LPE technique, the chosen solvent must be either suitable [8,9] or by adding surfactant [6,14,38–40] and, or polymeric solutions [12,13,41,42], so as to stabilize the nanosheet against re-aggregation [15]. Unlike the other above-mentioned preparation techniques, to synthesize high-quality MoS_2/graphene heterostructures by means of LPE method is a challenging task [24,43,44,45,46]. The conventional LPE synthesis technique has some drawbacks, including high defect rates, low stability, and compromised electronic properties. Additionally, the solvents utilized in exfoliation sometimes, can be toxic and alter the properties of the materials chemically [47,48]., as a result, Thus, a suitable synthesis approach that is environmentally friendly is preferred to make it practical for usage. This work modified the conventional LPE technique by including a pre-treatment process and employing an environmentally friendly isopropanol (IPA)/water solvent. This procedure was followed by a sequential deposition technique for the fabrication of vertical MoS_2/graphene heterostructure (photodetection).

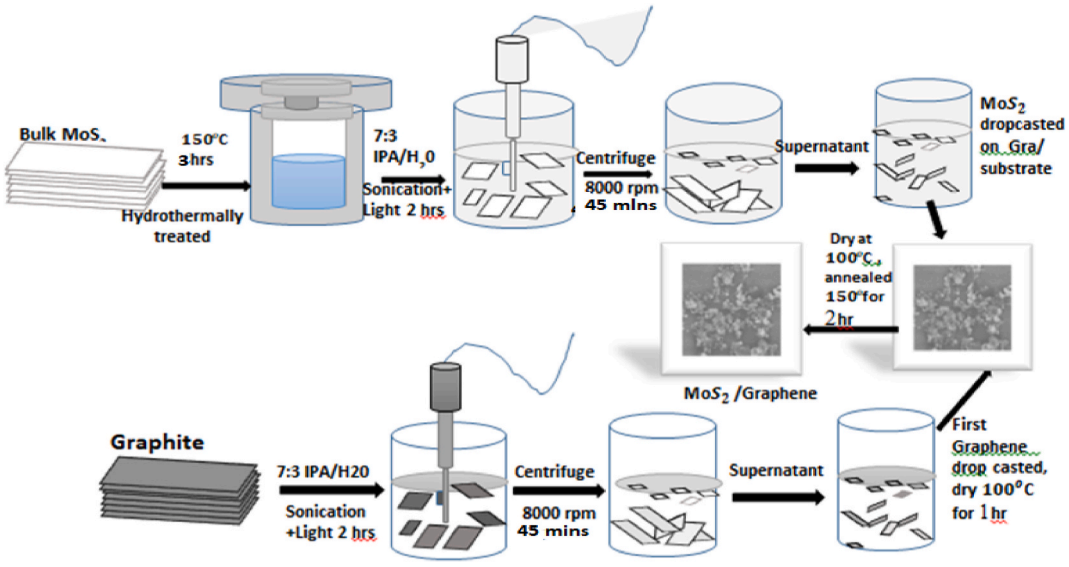

Fig. 1. Schematic method of preparation of MoS_2/graphene heterostructure.

2. Experiment

2.1. The synthesis of MoS_2, graphene, and MoS_2/Graphene heterostructure from a modified LPE technique

Graphene and MoS_2 dispersion were prepared using the improved LPE method as described in Ref. [5]. MoS_2 and graphite powders were supplied by Sigma and were of analytical grade (99 %). A micron-sized filtration system was used to obtain deionized (DI) water (Resistivity 18.2 MΩcm at 25 °C) from millique filtration system. First, MoS_2 was prepared by the hydrothermal process as follows; A solution of MoS_2 (<6 μm) was made by dissolving 0.4 g of MoS_2 in 30 ml of DI water followed by sonication for 1 h until a uniform mixture was obtained. The mixed solution was poured into a 100 ml Teflon liner and then enclosed in a tightly screwed stainless-steel jacket. The whole assembly is then heated for 3 h at 150 °C with continuous stirring. Exfoliation of the pre-treated MoS_2 was done by dispersing it in a 170 ml solution containing IPA and DI water mixed in a volume-to-volume ratio of 7:3, respectively.

The MoS_2 dispersion was ultrasonicated in iced water for 2 h using a sonic tip attached to a horn probe (Sonic VCX 750), as shown in Fig. 1. The ultrasonic irradiation was pulsed at 3 s interval between on and off states to avoid damaging the ultrasonic processor and prevent solvent heating, which could lead to the degradation of the MoS_2 nanosheets. After the sonication process, centrifugation of the black dispersion was then carried out at 8000 rpm for 45 min to separate the supernatant from the residue. The residue was discarded while the supernatant was subjected to further centrifugation process in order to completely remove the un-exfoliated powder and aggregates of MoS_2. A similar procedure was used to produce graphene, except for the initial hydrothermal treatment. Here, a graphite dispersion was formed by spreading 0.4 g of graphite powder into a mixture of IPA and DI water. The dispersion was then exfoliated as described above for 2 h, followed by centrifugation at 8000 rpm for 45 min and the resultant supernatant collected inside a beaker. The exfoliated products (graphene and MoS_2) were drop-cast on separate Si/SiO_2 substrates as follows; 10 μg/L graphene or MoS_2 solution was deposited on Si/SiO_2 substrate drop-wise and dried at 100 °C. The heterostructure of graphene/MoS_2 was produced by a sequential deposition of graphene and MoS_2 dispersions on the substrate using the drop casting approach. Solvent was evaporated at 100 °C for a duration of 1 h in-between each deposition. Lastly, the graphene/MoS_2 heterostructure was annealed at 150 °C for 2 h.

2.2. Fabrication of interdigitated electrode and photodetector device

The glass substrate was cleaned using acetone and IPA, sonicated for 10 min, and then washed with DI water with a purpose of removing impurities. A shadow mask that was designed and fabricated with interdigitated finger separation of 5 μm was placed into close contact with a glass substrate and mounted in a thermal evaporator chamber for metal deposition. The pressure in the chamber was lowered until it reached approximately 1×10^6 mbar. A standard thickness of 5 nm/50 nm of Cr/Au metal was used to create a metal contact on a glass substrate. The shadow mask was then allowed to cool for 24 h after deposition on the glass substrate. The metal contact was left on the glass substrate as the shadow mask was gently lifted and removed. The contact electrodes were bonded with any conducting connector using silver epoxy.

The fabricated inter-digitated electrodes (IDE) with the dispersion of the nanomaterials were used to fabricate the two photodetector devices: MoS_2 and MoS_2/graphene hybrid photodetector. The graphene dispersion was first deposited on the interdigitated electrode assembly and dried at 100 °C for 1 h. Then, MoS_2 dispersion was later deposited on the graphene/glass interdigitated

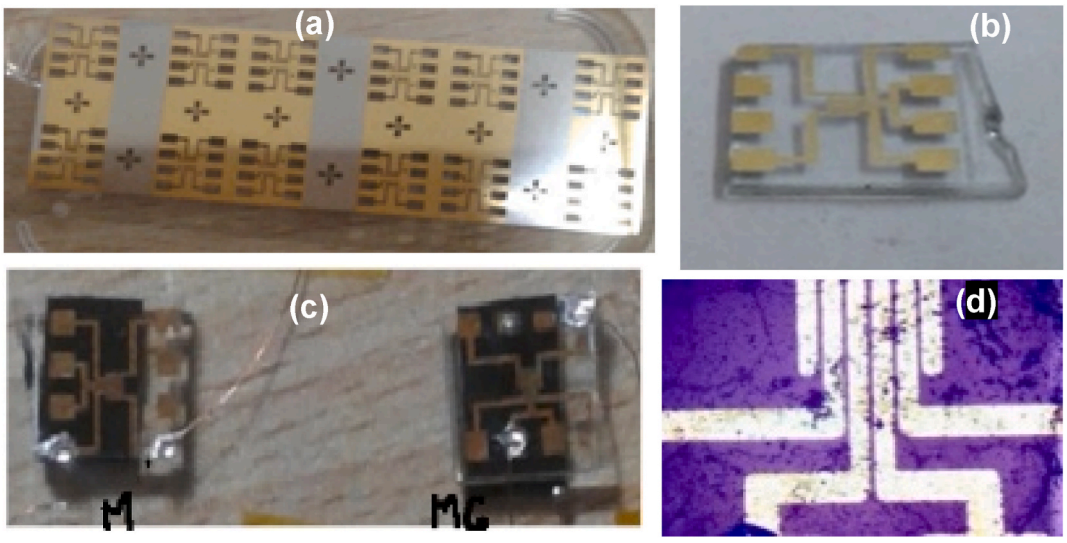

Fig. 2. (a). The designed shadow mask with finger separation of 5 μm, (b) fabricated IDE without any sample, (c) IDE with sample material, and (d) enlarged image of the samples laid across the metallic electrode.

electrode sequentially, followed by drying at 100 °C and then annealing under an argon atmosphere at 150 °C for 2 h. This step is meant to reduces the level of impurities that may be present in the samples at the exfoliation stage. Likewise, MoS_2 dispersion was deposited on the glass interdigital electrode using the procedure described above. Fig. 1 shows the schematic diagram for the preparation of MoS_2/graphene heterostructure. Fig. 2a shows the shadow mask which was designed and fabricated with interdigitated finger separation of 5 μm. Fig. 2b shows the digital image of the fabricated interdigital electrode without any sample, and Fig. 2c shows the fabricated device which consist of MoS_2 (M) and MoS_2/graphene heterostructure (MG). Fig. 2d display the zoom image of the samples laid across the metallic electrode; demonstrating that the contacts of the sample are intact.

2.3. Characterisation and measurement

Different techniques were used for characterization of the synthesized layers of MoS_2/graphene. The Shimadzu UV-2550 spectrophotometer was used measure the absorbance of the nanosheets and derive other optical parameters from it. The Horiba LabRAM HR Raman spectrometer was used to obtain Raman spectra at room temperature to detect modes of molecular motion and vibration in the layered materials. For structural analysis and mapping, the Titan Themis 300 KV transmission electron microscopy (TEM) from FEI was employed. The atomic force microscope (AFM), specifically the Park AFM NX 20 system, was used to measure thickness and sizes of the materials.

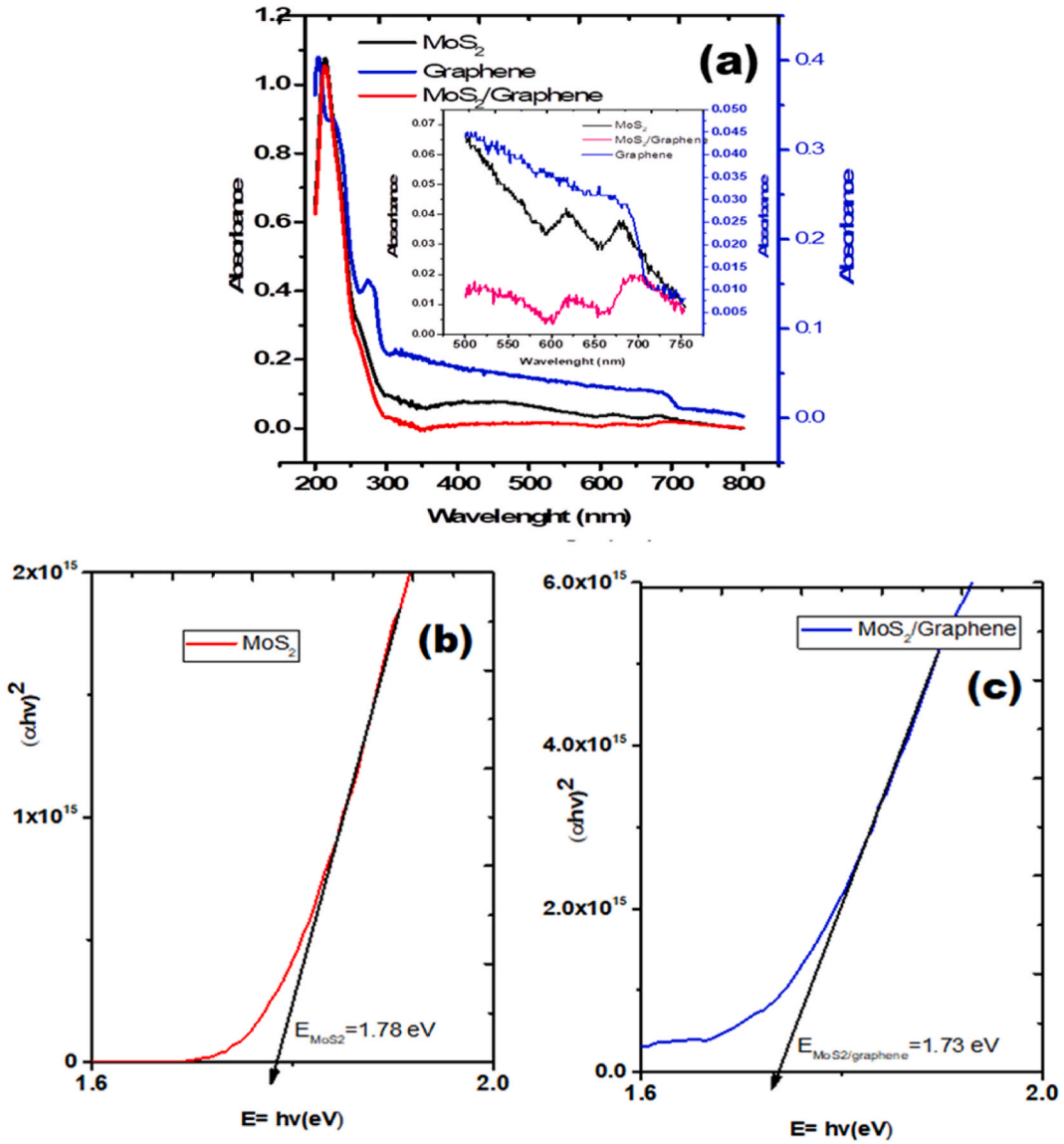

Fig. 3. (a) Absorbance spectra of exfoliated graphene, MoS_2, and MoS_2/graphene heterostructure, (b) Energy gap of exfoliated MoS_2, (c) Energy gap of MoS_2/graphene heterostructure. Inset is the magnified section of Fig. 3(a) in the range 500–750 nm.

Surface framework and elemental compositions of the nanosheets were determined using Ultra55 (Karl Zeiss) field emission scanning electron microscope (FE-SEM) coupled with energy dispersive X-ray spectroscopy (SEM-EDX). The electrical characteristics of the fabricated photodetector were assessed at room temperature in an air ambient using a meter source, specifically the Keithley 2400.

3. Results and discussion

3.1. UV–visible spectroscopy analysis

Fig. 3a shows absorption spectra of MoS_2 dispersions with two distinct absorption peaks; peat A at ~688 nm and peak B at ~625 nm. These observed absorption peaks are attributed to the direct inter-band excitonic electronic transitions within the material, specifically at the K point of the Brillouin zone in 2D MoS_2 [49,50]. These two excitonic peaks are also due to interaction between the spin-orbit splitting and layer contact. The splitting value, approximately 64 nm at 0.17 eV, agrees with other literature [51,52]. These distinctive peaks characteristics revealed a well-dispersed MoS_2 material with a 2H crystal structure [53]. Graphene has a strong absorption peak situated at about 272 nm (peak C). This peak C is frequently attributed to the π-π* absorption band of graphene and π-plasmon resonance band which emerges from a combined oscillation of π-electrons in the graphene lattice in riposte to incident light. The UV band at 272 nm makes it obvious that the graphene sample is composed of both thick multilayered and thin layered graphene [54]. The absorption spectra of MoS_2/graphene heterostructures prepared in this work have shown comparable absorption bands at 685 and 624 nm identical to those of exfoliated MoS_2 [51,54,55]. We observed a blue shift at the 685 and 624 nm for the heterostructure relative to the MoS_2's absorption bands. The MoS_2/Graphene heterostructure has complex interactions between the electronic structures, band alignments, and light-matter interactions of MoS_2 and graphene [34,42,51]. The energy bandgap of MoS_2 and MoS_2/Graphene heterostructures is depicted in Fig. 3b according to Tauc plot using Equation (1) [56,57,58,59].

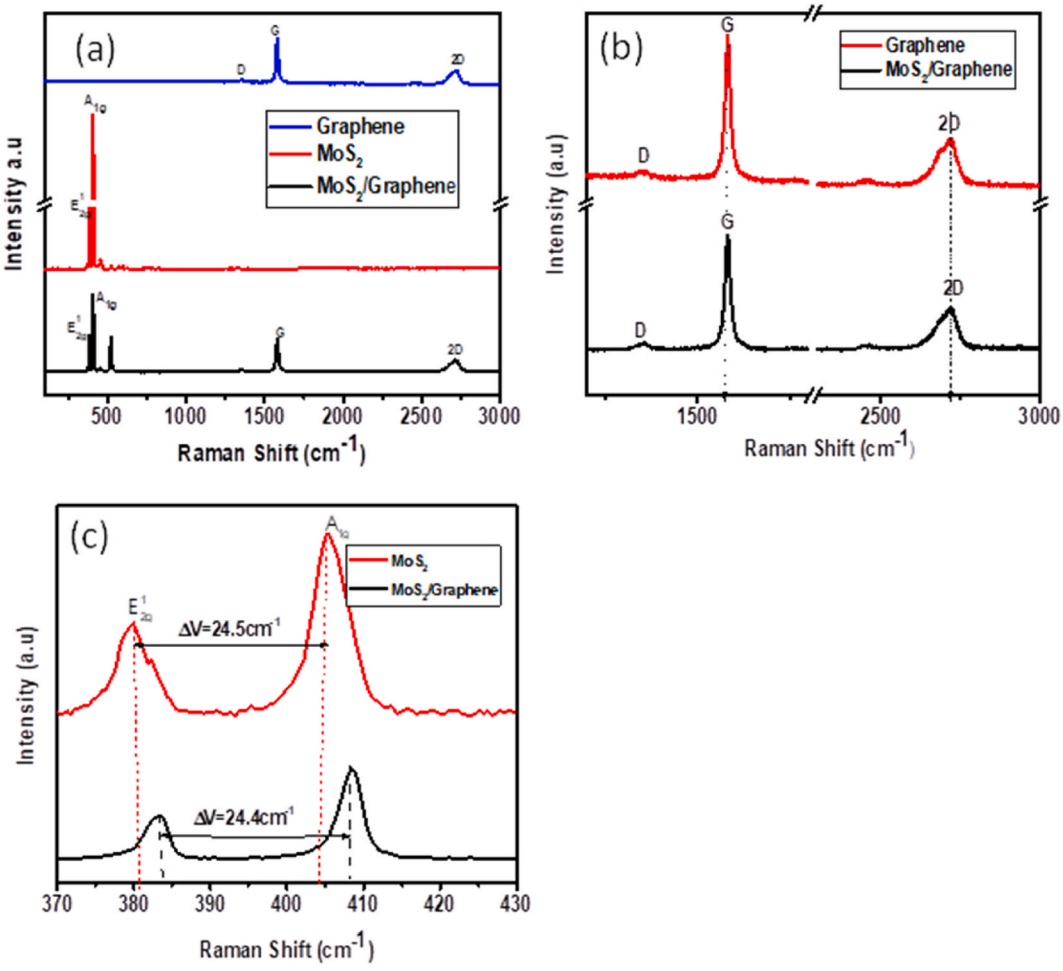

Fig. 4. (a) Display Raman spectra of exfoliated graphene, MoS_2, and MoS_2/graphene heterostructure, (b) enlarged Raman spectra of exfoliated graphene and MoS_2/graphene heterostructure, and (c) enlarged Raman spectra of exfoliated MoS_2 and MoS_2/graphene heterostructure.

$$(\alpha h\nu) = \beta\left(h\nu - E_g\right)^n \quad (1)$$

where α, β, ν, n, and h denote the absorption coefficient, band tailing constant parameter, frequency, power factor, and Planck's constant, respectively. $h\nu$ represents the energy of incident photon, E_g the optical band gap, while n is a power factor that depends on the allowable optical transitions, which have the direct and indirect transitions correspond to n values of 1/2 and 2, respectively. The plot of $(\alpha h\nu)^n$, where n is 2, versus $h\nu$ gives a straight line [56,57,58,60]. When the straight line is extrapolated to intercept the $h\nu$ axis, the MoS_2's optical energy band gap values is 1.78 eV while for MoS_2/Graphene heterostructure is 1.73 eV. (see Fig. 3b and c). The obtained band gap value of MoS_2 synthesized in this work is comparable to the previously described value for a direct band gap MoS_2 of a few nanosheets [37,61].

3.2. Micro-Raman spectroscopic

Fig. 4a shows Raman spectra of the three different materials: MoS_2 nanosheets, graphene nanosheets, and MoS_2/graphene heterostructure. The Raman peaks in the spectra of the graphene nanosheet revealed the D, G, and 2D bands, with their corresponding wavelengths at 1347, 1575, and 2701 cm^{-1}. The D band is a characteristic feature of structural defects in carbon materials. The Raman spectrum exhibits weak D band at 1347 cm^{-1}, indicating reduced carbon material structural defects. The G band at 1575 cm^{-1} (see Fig. 4b) is attributed to E_{2g} mode at the k-point as a result of the C–C bond stretching in graphitic materials. This phenomenon is a usual occurrence all sp^2 carbon systems. The Raman spectra of MoS_2 showed two separate peaks at 380 and 404.5 cm^{-1} which correspond to the in-plane opposite vibrations of S–Mo atoms mode and the out-of-plane stretching of the sulphur, respectively. Raman active modes of MoS_2 [18,62]. Upon interacting with the layers of MoS_2 and graphene, the Raman-active phonon modes offer valuable insights into how the two materials interact between each other. The Raman spectra observed at 383, 407, 1346, 1573, and 2700 cm^{-1} in the heterostructure are ascribed to the combined vibronic bands of MoS_2 and graphene. However, the peak positions have shifted towards higher wave numbers as shown in the enlarged section shown in Fig. 4c. This shift may have been caused by heterostructure forming which is known to affect the out-of-plane vibrations.

The intensity ratio, I_D/I_G for the MoS_2/graphene heterostructure and graphene were estimated to be 0.2092 and 0.1680,

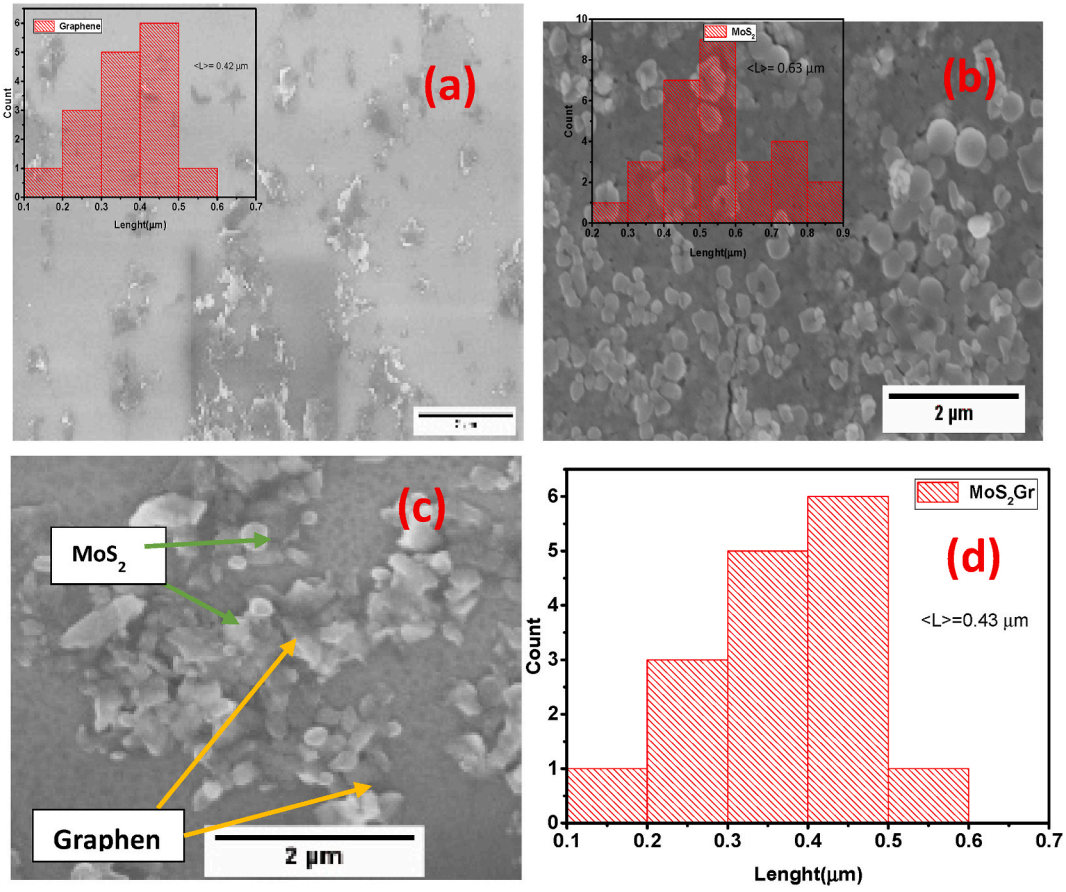

Fig. 5. SEM images of (a) graphene nanosheets, (b) MoS_2 nanosheets, (c) MoS_2/graphene, and (d) histogram of sheets sizes for MoS_2/graphene. All insets are histograms showing the lateral size distributions in corresponding images.

respectively. The high intensity ratio for the heterostructure indicates more defects in the material compared to graphene nanosheets. Conversely, the ratios of I_{2D}/I_G for graphene nanosheets and MoS_2/graphene heterostructures are 0.41 and 0.42, suggesting the existence of a graphene with few layers and a heterostructure. MoS_2 nanosheets layer number can be determined by considering the wavelength of the Raman peaks and their separation [6,24]. In the enlarged Fig. 3c, the Raman spectra show the two distinct at 380 cm^{-1} and 404.5 cm^{-1} for MoS_2 nanosheets, while for the MoS_2/graphene heterostructure, the peaks were red-shifted to 383 and 407.4 cm^{-1}. The peak upshifts of 3.0 cm^{-1} are said to be caused by a decrease in the interlayer van der Waals force, while the A_{1g} peak upshift of 2.9 cm^{-1} provides proof for the effectiveness of the interfacial interaction [62]. It is well reported that the location of the waves and their wavenumber difference are sensitive to the sheet thickness only when the layer number is less than four (<4) [62]. The presence of few layers (<4) is confirmed by the wavenumber difference of ~24.5 cm^{-1} measured between the distinctive peaks of MoS_2 (Fig. 4c) [62,63]. However, a wavenumber difference of ~24.4 was obtained for the MoS_2/graphene heterostructure.

3.3. Morphology and structural analysis of exfoliated nanosheets

3.3.1. SEM micrographs and elemental mapping

Fig. 5 shows SEM micrographs of exfoliated graphene, MoS_2 nanosheets, and MoS_2/graphene heterostructure. A flake-like shape of the exfoliated graphene is clearly observed in Fig. 5a. The estimated average size of graphene nanosheets using the histogram in the inset of Fig. 5a–is 420 nm. Also, MoS_2 nanosheet SEM images are sheet-like with a circular shape, its average size of 630 nm was also obtained from the histogram in the inset of Fig. 5b. Fig. 5c and d, respectively, display the size distribution and SEM micrograph of the as-synthesized MoS_2/graphene heterostructure. The heterostructure's estimated average size was 430 nm. Fig. 5c shows an assemblage of a homogeneous distribution of graphene and MoS_2 with interconnections between them. Most of the graphene nanosheets are covered by MoS_2 nanosheets. The MoS_2 nanosheets are observed to be uniformly distribution on the graphene nanosheets as displayed by the elemental mapping in Fig. 6a-f. It is also seen Fig. 6a-f that the MoS_2/graphene heterostructure show a homogeneous distribution of C, O, Mo, and S.

3.3.2. Atomic force microscopy analysis

Atomic force microscopy images of graphene, MoS_2, and MoS_2/graphene heterostructure nanosheets are presented in Fig. 7(a)-(c). Like in the case of SEM, the AFM image of graphene nanosheets (Fig. 7a) has elongated flake-like shapes. The MoS_2 nanosheet displayed in Fig. 7b has tiny, nearly spherical shaped particles uniformly distributed on the substrate. Meanwhile, Fig. 7c shows a mixture of flake-like particles and spherical particles, signifying a hybrid of graphene and MoS_2 particles in the heterostructure. Fig. 7(d)–(f) represent the thickness distribution of exfoliated graphene, MoS_2 and the heterostructure. The average flake thicknesses for graphene, MoS_2, and MoS_2/graphene heterostructures are 5.5, 2.8, and 4.1 nm, respectively. Though it is improbable to have both the largest and smallest flakes in a distribution, these are not definite limits for the thickness since only a small drop of the sample was used for this

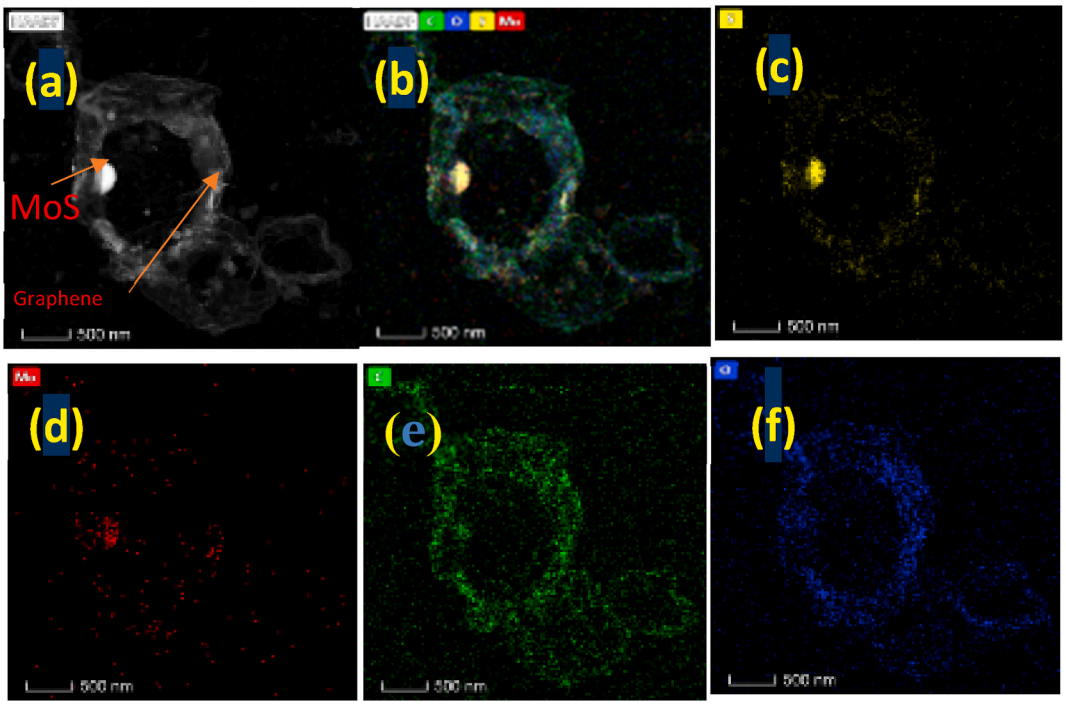

Fig. 6. Elemental maps showing distribution of elements in MoS_2/graphene heterostructure nanosheets.

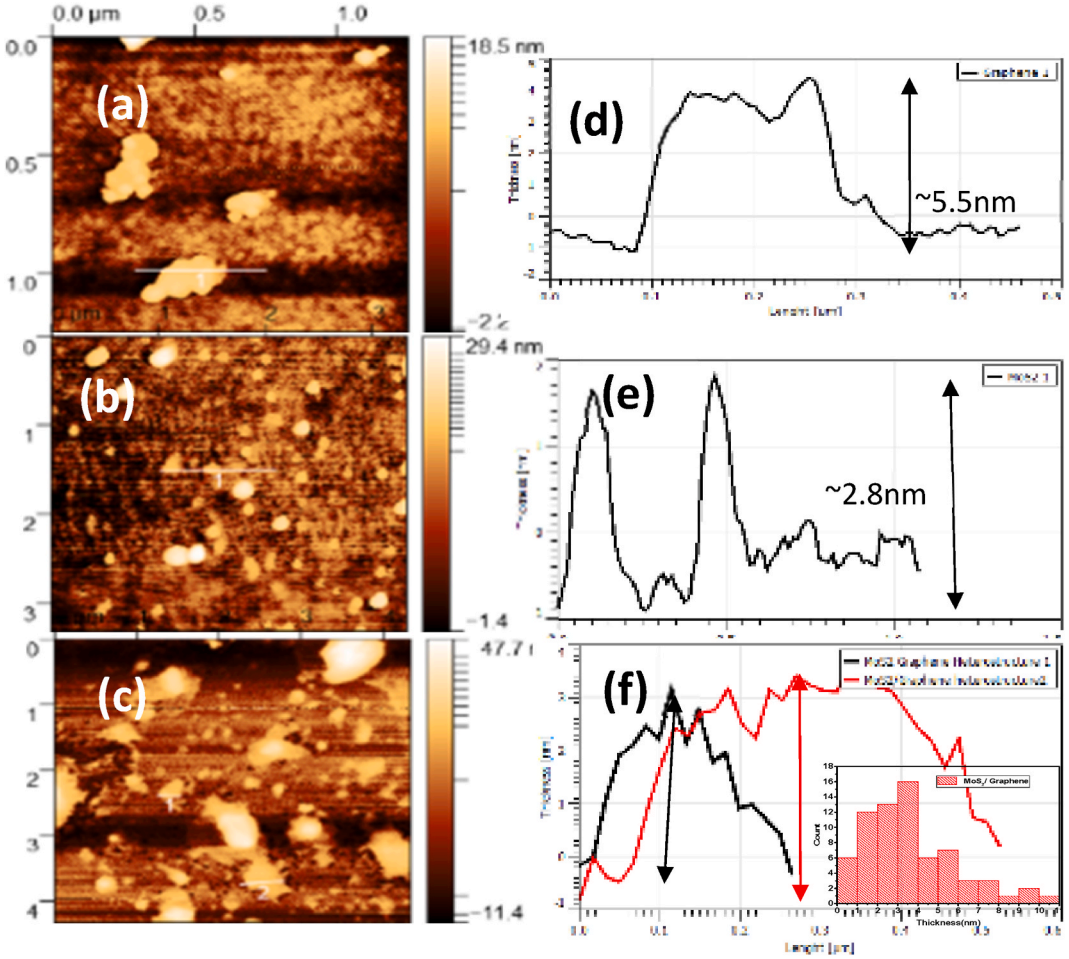

Fig. 7. AFM images of (a) graphene nanosheets, (b) MoS_2 nanosheets, and (c) MoS_2/graphene heterostructure, while (d)–(f) Represent the corresponding thickness distributions of particles in the AFM images, respectively.

characterization. Therefore, a little population of nanosheets beyond these bounds probably exists. As shown by the AFM images, the small thickness of nanosheets of MoS_2 and graphene with their heterostructure strongly confirm that the few layers of the materials were successfully exfoliated by this improved liquid phase exfoliation technique.

3.3.3. Microstructural analysis of exfoliated nanosheets

The XRD patterns of exfoliated graphene presented in Fig. 8 have two diffraction peaks situated at 2θ positions 26.5° and 54.6° which corresponds exactly to the (002) and (004) planes of graphene and matches with JCPDS card No 75–1121. The d-spacing of exfoliated graphene is 0.3358 nm, calculated using the Bragg equation, which is larger than that of graphite (0.334 nm) [11]. Also from the same Fig. 8, the XRD pattern of an exfoliated MoS_2 nanosheet presents diffraction peaks at 2θ angles of 14.32°, 28.11°, 32.07°and 44.08 which was indexed to the (002), (004), (100), and (006) planes respectively which is in accordance with the pure hexagonal ($P6_3/mmc$ space group phase of MoS_2 (JCPDS card no.06-0097) [35,40]. In addition, the peak at (002) is broad compared to others, indicating that the lateral size of MoS_2 [36]. The X-ray diffraction peaks of both MoS_2 and graphene appear in the MoS_2/graphene heterostructure, indicating a formation of a hybrid structure.

3.3.4. TEM analysis of exfoliated nanosheets

The TEM images in Fig. 9a and b displays agglomerated particles with no distinct morphology at low magnification for MoS_2 and MoS_2/graphene heterostructures, respectively. However, there is a clear view of lattice fringes for individual particles in the HRTEM images of Fig. 9c and d, which have lattice spacing for MoS_2 and MoS_2/graphene heterostructure of 0.27 nm and 0.33 nm, respectively. These values for lattice spacing were confirmed using Fast Fourier Transform, FFT generated from the diffraction fringes of the HRTEM images. The selected area electron diffraction (SAED) patterns were also obtained for the MoS_2 and MoS_2/graphene heterostructures so as to verify the existence of crystallinity and structure in the nanosheets. These patterns are shown in Fig. 9e and f, respectively. The SEAD pattern revealed the in-plane hexagonal atomic composition of the samples, which confirms the crystallinity of the exfoliated

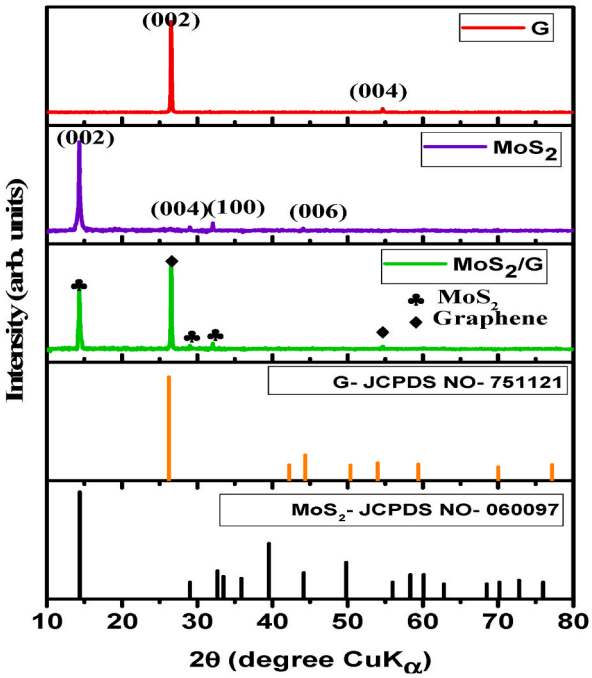

Fig. 8. The stacked X-ray diffraction patterns of graphene nanosheets, MoS_2 nanosheets and MoS_2/graphene heterostructure.

nanosheets. Again, the (002) plane projection shows that MoS_2, graphene, and their composite have well-stacked layered structure along a specific orientation. A similar pattern was noted in the XRD, indicating that the as-synthesized nanosheets are composed of a few-layers.

3.3.5. *Current-voltage characteristics of the fabricated photodetectors*

Fig. 10a and b displays the current-voltage (C–V) characteristics of the photodetectors under 650 nm illumination conditions (1–3 mW/cm^2) and dark conditions. The linear increase in current with increasing illumination intensity observed in Fig. 10a and b can be attributed to a good ohmic nature of semiconductor/Au junction for both detectors. Ohmic contacts allow charge carriers to easily flow from the material's conduction band to the Au metal conversely by tunneling, which in turn enables strong photocurrent generation [64]. The injection of the carrier into electrodes can be achieved effectively through voltage biasing which in turn give rise higher mobility and current density. The chemical bonding between sulphur in MoS_2 and gold atoms at the flake edges is the reason for the very small potential barrier at MoS_2/Au interface [51]. In MoS_2/graphene photodetectors, graphene is much more conductive than MoS_2. When MoS_2 and graphene are in contact, the resistance increases, indicating passive electron transfer from MoS_2 to graphene [52]. Also, a greater photoresponse is achieved through the integration of the high optical responsivity of MoS_2 with the excellent electronic transport capability of graphene. Because graphene is more conductive, so it dominates carrier transport in the resulting.

These types of photodetectors work by picking up variations in the layer's intrinsic conductance when a nanosheet's active layer is exposed to light. They can effectively separate and extract photo-excited charge carriers due to their high sensitivity to light [64]. To calculate the photocurrent (I_{ph}), the dark current (I_D) is deducted from the illumination current (I_L) which is represented by the equation: $I_{ph} = I_L - I_D$. Fig. 10c and d depict the transient response of the photodetectors observed under 1 mW/cm^2 for MoS_2 and MoS_2/graphene photodetectors, respectively. This was achieved by simply applying a 4 V constant bias and varying the power intensity of the 650 nm illumination by turning it on and off periodically. The device produced a photocurrent of 0.55 μA, which is an excellent result for MoS_2 detector and 3.55 μA for MoS_2/graphene detector. Besides, the devices showed good response to variations in illumination, this is an important characteristic of a photodetector. We further measured the response time of the photodetectors, that is, the duration required for the current to shift from 10 % to 90 % (rise time) and vice versa (decay time). Fig. 10e and f illustrate the response time of MoS_2 and MoS_2/graphene detectors, respectively. Also, the rise (τ *rise*) and decay (τ *decay*) times for MoS_2 and MoS_2/graphene detectors were found to be 1.0 s/1.22 s and 0.9 s/1.02 s, respectively.

The photocurrent's variation with illumination intensity is depicted in Fig. 11a. The enhancement of photocurrent occurs as the light intensity rises from 1 to 3 mW/cm^2. For the MoS_2 base detector, the photocurrent increased from 0.55 to 1.61 μA. for the MoS_2 base detector, the photocurrent increased from 0.55 to 1.61 μA and for the MoS_2/Graphene based-photodetector, the increase in photocurrent is from 3.55 to 8.92 μA. Both MoS_2-based and MoS_2/graphene-based detectors exhibit a positive dependence on the incident power intensity. This is because the number of photogenerated charge carriers are increased with increasing incident power intensity, which results in effective electron-hole separation and recombination in the photodetectors. The mechanism works like this: when light is absorbed, it generates effective electron-hole pairs. These pairs then undergo separation and recombination under bias

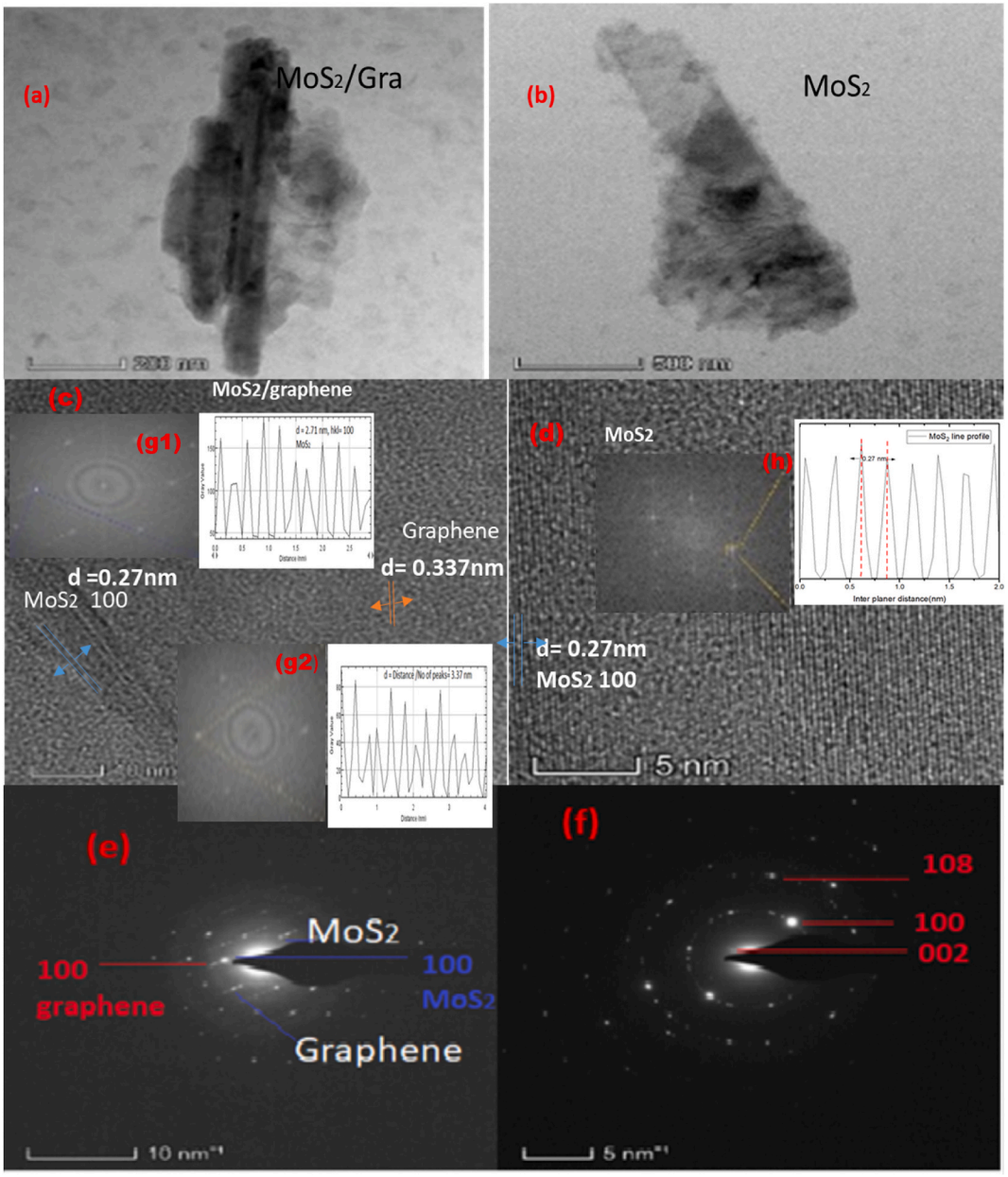

Fig. 9. TEM images of (a) MoS_2/graphene, (b) MoS_2, and (c) and (d) are their corresponding HRTEM images, (e) and (f) are SAED patterns of the prepared nanosheets. In the inset are FFT of the diffraction fringes in the HRTEM images.

voltage. This generates an electric field at the gold/graphene nanosheets interface and another electric field is produced at the MoS_2/graphene interface due to the bias. The generation of these electric fields plays a significant role in the separation charge carriers and the subsequent transfer of these carriers to the electrodes, which enhances the photoconductive behavior of MoS_2/graphene-based photodetectors [54]. The presence of two electric field generating interfaces in MoS_2/graphene photodetector is the reason for the higher photocurrent for this device when compared with the MoS_2-based detector.

To further study the optoelectronic performances of MoS_2 and MoS_2/graphene photodetectors, the responsivity, R, specific detectivity, D* and external quantum efficiency, EQE of the photodetectors were determined for wavelength at 650 nm. The photo-responsivity is obtained by taking the ratio of the photocurrent ($I_{ph} = I_L - I_D$) to the illumination power absorbed by the photodetector, and is obtained from Equation (2):

$$R = I_{ph}/P_{in} \tag{2}$$

where I_{ph} is the photocurrent and P_{in} is the incident power on the photosensitive zone.

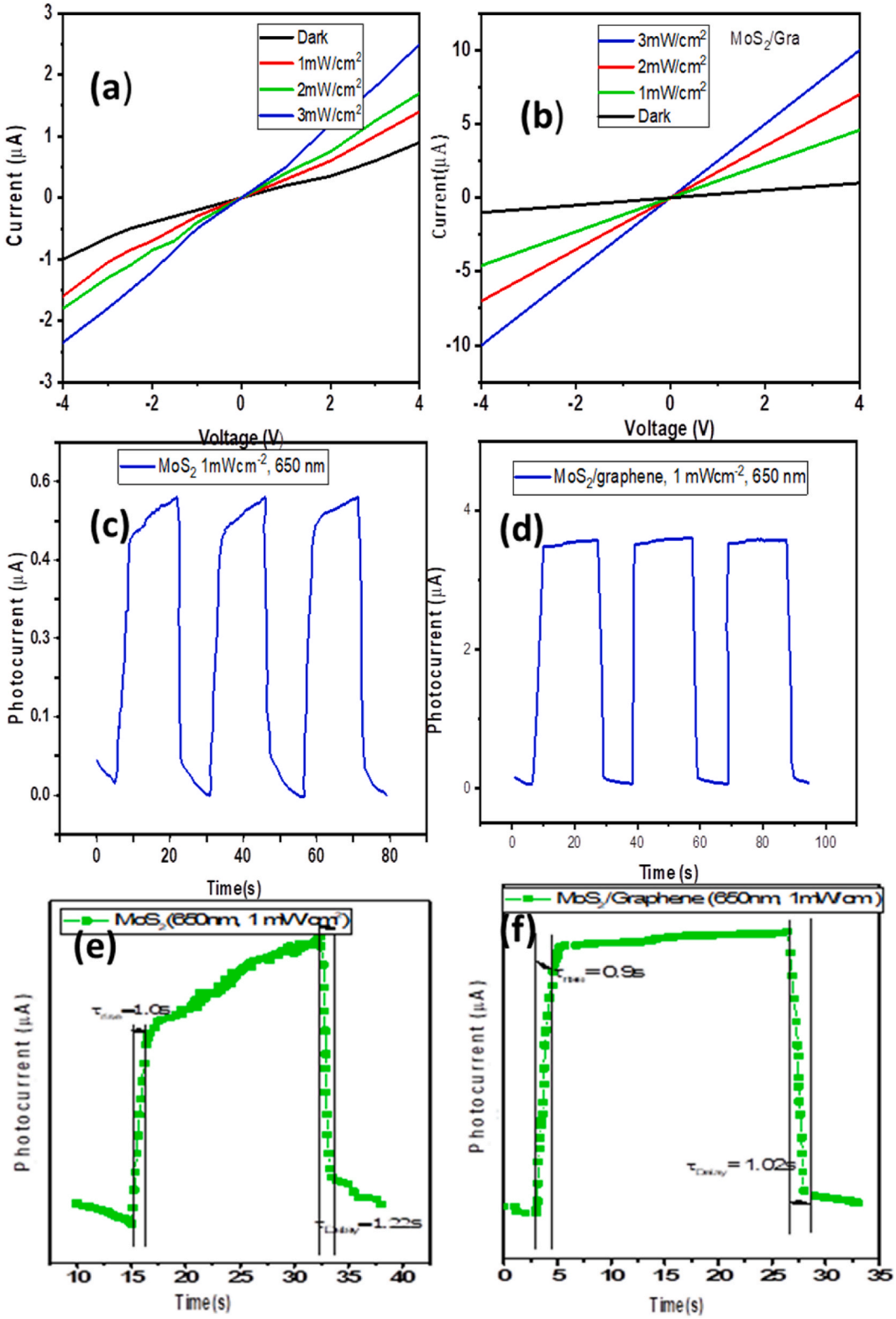

Fig. 10. (a & b) I–V characteristics, (c & d) transient photocurrent, and (e & f) time trace measurement of MoS_2 and MoS_2/Graphene (MoS_2/Gr) photodetector under dark and 650 nm illumination.

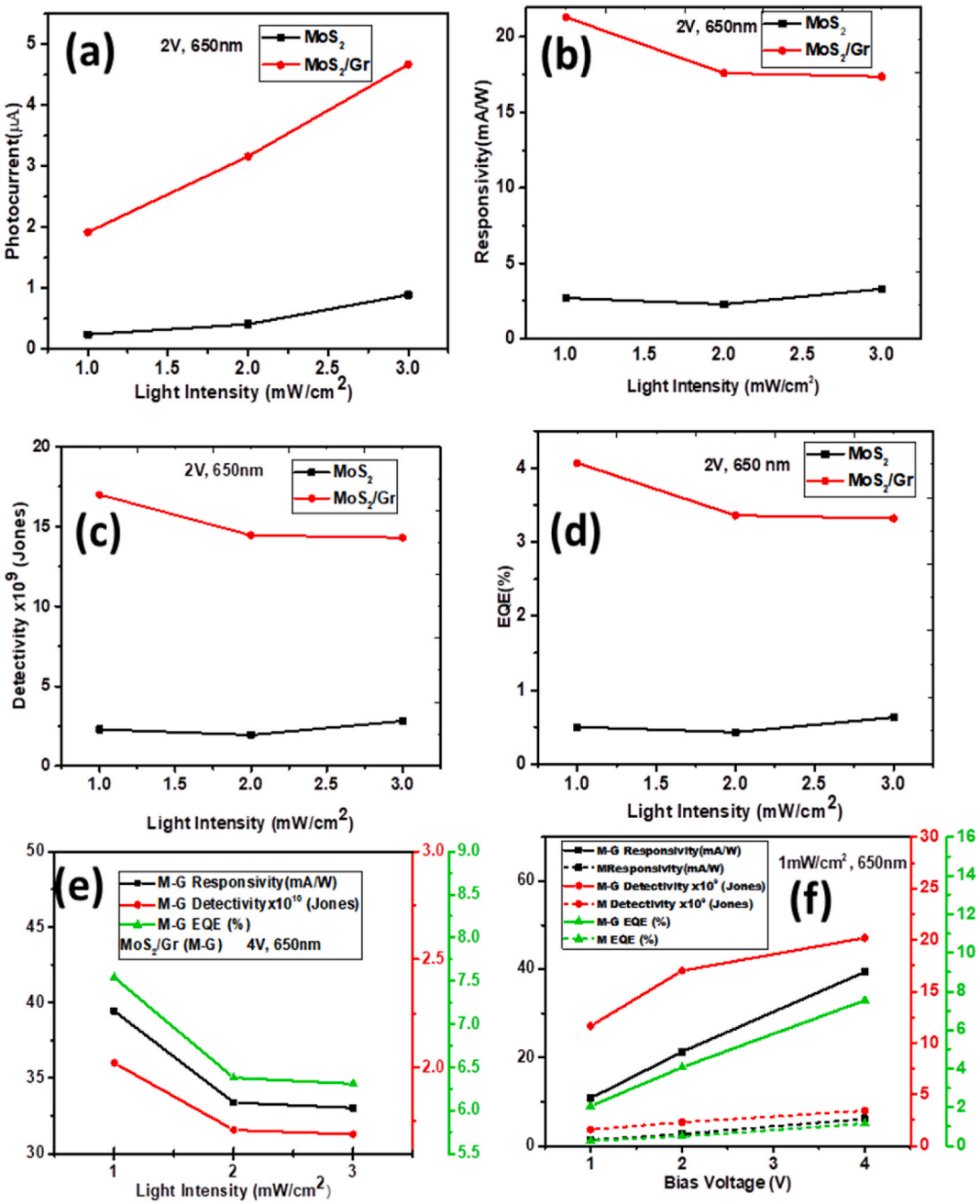

Fig. 11. Variation of photocurrent (a), photoresponsivity (b), specific detectivity (c), and EQE (d) with light intensity at 2 V; (e) combination of parameters (a)–(d) at 4 V; and (f) combination of parameters (a)–(d) under bias voltages ranging from 1 to 4V for MoS_2 and MoS_2/Graphene (MoS_2/Gr).

Fig. 11b illustrates the photoresponsivity of MoS_2 and MoS_2/graphene photodetectors. The photoresponsivity values range between 2.7 and 3.3 mA/W and 17.4–21.3 mA/W, respectively. These values were obtained using a bias voltage of 2 V, 650 nm wavelength, and with light power intensity in the range approximately 1 mW/cm^2 to 3 mW/cm^2. In the photodetectors, increase of the effective power intensity is associated with decrease of their photoresponsivities. Iincreasing incident power intensity generates additional photo-carriers, which may recombine or be caught in traps, reducing photoresponsivity [65–67].The specific detectivity of the photodetector was determined using Equation (3). The specific detectivity, is defined as a normalized measure of its lowest detectable light power [68]. Its units of Jones ($cm^{-1}Hz^{1/2}\ W^{-1}$),

$$D^{*} = R\sqrt{\frac{A}{2eI_{dark}}} \tag{3}$$

where e, A, R, and I_{dark} are the unit charge, photosensitive area, responsivity and the dark current, respectively.

Meanwhile, the external quantum efficiency (EQE) of the fabricated photodetector was computed using Equation (4):

$$EQE = \frac{electrons/sec}{photon/sec} = \frac{Rhc}{e\lambda} \times 100\% \tag{4}$$

where h, c, and λ are the Planck's constant, speed of light, and wavelength of illumination, respetively. Fig. 11c and d shows the plot of detectivity versus illumination intensity and EQE against illumination intensity, respectively. From these figures and using equations (3) and (4), the computed values of detectivity (and EQE) are 2.29×10^{9} Jones (and EQE = 0.5 %) and $1.7 \text{ x} \times 10^{10}$ Jones (EQE = 3.32 %) for MoS_2 and MoS_2/graphene photodetectors, respectively under a biased voltage of 2V at 650 nm illumination. Interestingly, the detectivity and responsivity of MoS_2/graphene photodetector is considerably greater than that of MoS_2 photodetector,

In Fig. 11e, the changes in MoS_2/graphene detector parameters are presented across a range of power intensities (1–3 mW/cm^2) under 650 nm light exposure with a 4 V biased voltage. The detector achieved a responsivity, detectivity, and EQE of 33.39 mA/W, 1.71×10^{10} Jones and 6.4 % at 650 nm and 4 mW/cm^2, respectively. The decline in responsivity at higher power intensity is linked to the constraint imposed by the trapping of photogenerated charge carriers at defects sites [4].

The photoresponsivity, detectivity, and EQE of the photodetectors demonstrate improvement with increasing bias voltage at 1, 2, and 4V, as illustrated in Fig. 11f. The rise in bias voltage corresponds with an increase in photoresponsivity, specific detectivity, and EQE for the detectors. Table 1 shows that the MoS_2/graphene detector parameters align with those of similar photodetectors reported by other researchers. However, the MoS_2/graphene detector crafted in this study using an enhanced liquid phase exfoliation method outperformed a similar detector fabricated solely through the LPE technique. Other methods such as hydrothermal and CVD are highlighted in Table 1.

3.3.6. 6: mechanism for MoS_2/Graphene photodetection and the defect trapping in MoS_2

The energy band diagrams presented in Fig. 12a and b outline the operational mechanism of the MoS_2/graphene photodetector. Upon the convergence of graphene and MoS_2, an interface emerges, establishing a potential barrier between them. This prompts the migration of electrons from MoS_2 to graphene until equilibrium is established, aligning the Fermi levels and creating a built-in electric field or potential barrier between the two materials. As graphene possesses a lower work function than the conduction band of MoS_2, electrons can smoothly transit to the graphene layer.

When MoS_2 is illuminated, it absorbs light, generating electron-hole pairs. These pairs undergo effective separation at the MoS_2/graphene interface due to the built-in electric field, as well as through the influence of charged impurities and adsorbates. Holes function as positive gates, and electrons serve as charge carriers. The exceptional carrier mobility of graphene and the extended charge-trapping lifetime of holes facilitate multiple recirculations of electrons within graphene, resulting in heightened photocurrent and photogain. In a direct performance comparison, the MoS_2/graphene device outshines the MoS_2 device.

The presence of defect states and adsorbents significantly impacts the photoresponse of optoelectronic devices. Schematic representations in Fig. 12c–e illustrate the dynamic processes in a defective semiconductor subjected to illumination. Initially, deep-level defect states (DLDS) in the semiconductor remain unoccupied in the absence of light (Fig. 12c). When exposed to light, Fermi-level movement leads to the trapping of electrons in defect states before reaching the electrode (Fig. 12d). The gradual filling and subsequent release of defect states during these processes influence the duration of the photodetector response [74]. The extended time required for photogenerated carriers to fill multiple defect states and or for filled defect states to release and discharge trapped electrons in TMDs materials contribute to the prolonged response time of the photodetector.

Table 1
A comparison of typical detectors parameters of the fabricated MoS_2/graphene photodetector with previously reported 2D MoS_2/graphene-based photodetectors.

Materials	Fabrication technique	Responsivity (A/W)	Detectivity (Jones) × 10^{12}	EQE (%)	Response Time (ms)	Ref.
MoS_2/graphene	Improved liquid phase exfoliation	0.0394	0.0202	7.5	900	This work
MoS_2/graphene	Solution processed	0.0033			0.88	[32]
MoS_2/graphene	Chemical vapour Deposition-	1.6×10^{4}	4.0	–	–	[69]
Graphene/MoS_2	Chemical vapour Deposition	$> 10^{7}$	0.0125	–	2100	[70] [71],
Graphene/MoS_2	Chemical vapour Deposition	~2.10	~0.5		200–18	[72]
MoS_2/graphene	Sputtering Chemical vapour Deposition	1.26×10^{5}	0.04.2	–	11	[73]
MoS_2/graphene	Chemical vapour Deposition	2.2×10^{5}	350	–	11	[71]

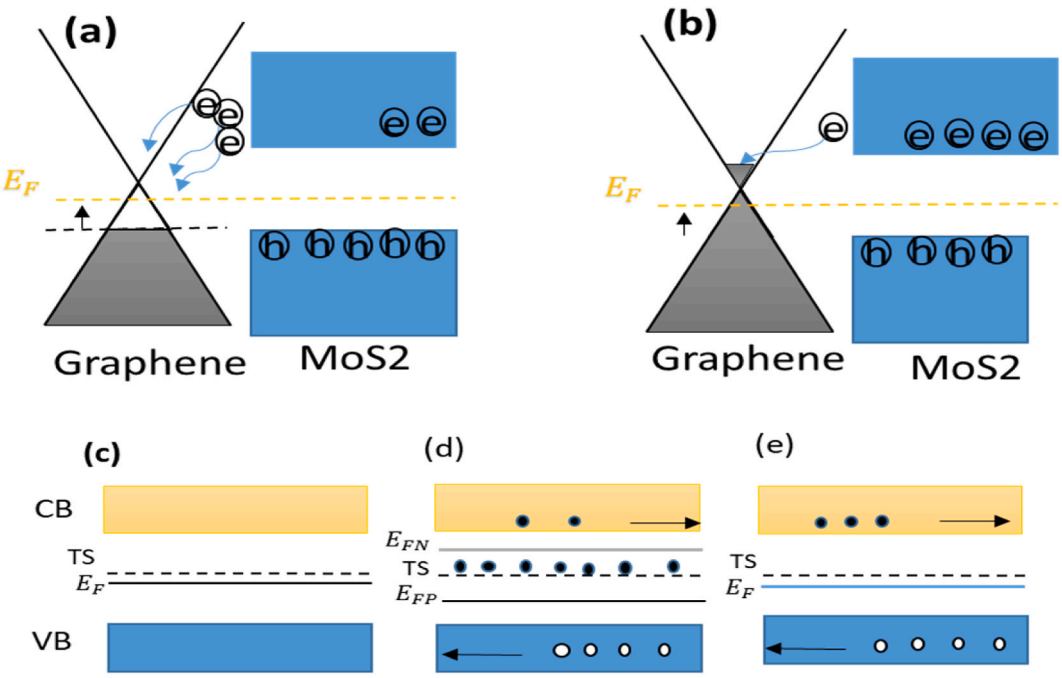

Fig. 12. The energy band diagram and schematic presentation of the photoelectron transfer process within the MoS_2/graphene heterostructure: (a) Electrons sourced from MoS_2 are introduced into graphene until the Fermi level achieves alignment during equilibrium. (b) The aligned Fermi level under equilibrium establishes a potential barrier (built-in electric field) between graphene and MoS_2. (c) In the absence of illumination, the localized defect states, specifically the deep-level defect state (DLDS) beyond the Fermi level in MoS_2, remain vacant. (d) When exposed to light, the Fermi level undergoes a shift to higher energy, causing electrons to be entrapped in defect states before reaching the electrode. (e) Following the cessation of illumination, Fermi-level electrons revert to their original position, leading to the gradual release and depletion of electrons from the defect states [67].

4. Conclusion

In summary, the present work focused on MoS_2 nanosheets, graphene nanosheets, and their composites and synthesized them by an improved liquid-phase exfoliation method. The heterostructure nanosheets were formed through sequential deposition technique for the fabrication of vertical MoS_2/graphene heterostructure. Morphological and microstructural characterizations of these nanosheets confirm that a few layers were exfoliated with thicknesses of 3 nm–5 nm and lateral sizes of 500 nm and 350 nm were prepared with good crystallinity. The fabricated MoS_2 and MoS_2/graphene heterostructures displayed good electrical characteristics. The MoS_2/graphene heterostructure device exhibits sensitive photoresponse at bias voltages of 2 V and 4 V for wavelengths of 650 nm. This sensitivity is observed across a range of light power intensities, spanning from 1 mW/cm^2 to 3 mW/cm^2. The MoS_2/Graphene photodetector has a response of 39.44 mA/W, relatively high specific detectivity of 2.02×10^{10} Jones, efficiency of 7.54 % at 4V bias voltage and that of MoS_2 photodetector are 6.11 mA/W, 3.4×10^9 Jones, and 1.16 %, respectively. Since the photoresponse performance of MoS_2/graphene photodetector is significantly improved over the sole MoS_2 photodetector device, it is a potential candidate for building future ultrasensitive devices. Besides, the MoS_2/graphene photodetector fabricated in this work using the improved liquid phase exfoliation technique showed better responsivity compared to MoS_2/graphene photodetector fabricated by other researchers. This research has provided a good, efficient, and cost-effective method with sequential deposition technique for fabricating MoS_2/graphene heterojunctions in order to enhance optoelectronic performance.

Funding

The authors declare that no funds, grants, or other support were received during the preparation of this manuscript.

Ethical approval

This declaration is not applicable.

Data availability

The data for this work will be made available on request.

CRediT authorship contribution statement

B.J. Akeredolu: Writing – review & editing, Writing – original draft, Visualization, Validation, Methodology, Investigation, Funding acquisition, Formal analysis, Data curation, Conceptualization, Writing – review & editing, Writing – original draft, Visualization, Validation, Project administration, Methodology, Funding acquisition, Formal analysis, Data curation, Conceptualization. **I. Ahemen:** Writing – review & editing, Validation, Supervision, Project administration, Formal analysis, Data curation, Conceptualization. **A.N. Amah:** Writing – review & editing, Validation, Supervision, Conceptualization. **A.D. Onojah:** Writing – review & editing, Validation, Supervision, Conceptualization. **Jyoti Shakya:** Writing – review & editing, Formal analysis, Data curation, Conceptualization. **H.N. Gayathri:** Writing – review & editing, Methodology, Formal analysis, Data curation, Conceptualization. **Arindam Ghosh:** Writing – review & editing, Validation, Supervision, Funding acquisition, Conceptualization.

Declaration of competing interest

The authors declare that they have no known competing financial interests or personal relationships that could have appeared to influence the work reported in this paper.

Acknowledgement

The authors are immensely grateful to Nigerian Tetfund and Indian Institute of Science, India for providing the research facilities.

References

[1] K.S. Novoselov, A.K. Geim, S.V. Morozov, D. Jiang, Y. Zhang, S.V. Dubonos, I.V. Grigorieva, A.A. Firsov, V. Grigorieva, Electric field effect in atomically thin carbon films, Science 306 (2004) 666–669.
[2] B. Adilbekova, Y. Lin, E. Yengel, H. Faber, G.T. Harrison, Y. Firdaus, A. Labban, D.H. El-Anjum, V. Tung, T.D. Anthopoulos, Liquid phase exfoliation of MoS_2 and WS_2 in aqueous ammonia and their application in highly efficient organic solar cells, J. Mater. Chem. C 8 (12) (2020) 5259–5264, https://doi.org/10.1039/D0TC00659A.
[3] Q. H Wang, K. Kalantar-zadeh, A. Kis, J.N. Coleman, M.S. Strano, Transition metal dichalcogenides, Nat. Publ. Gr. 7 (2012) 699–712.
[4] A.O. Neill, U. Khan, J.N. Coleman, Preparation of high concentration dispersions of exfoliated MoS_2 with increased flake size, Chem. Mater. 24 (2012) 2414–2421.
[5] J. Shakya, H.N. Gayathri, A. Ghosh, Defects-assisted piezoelectric response in liquid exfoliated MoS_2 nanosheets, IOP nanotechnology 33 (2022) 075710.
[6] A. Adetayo, D. Runsewe, Synthesis and fabrication of graphene and graphene oxide : a review, Open J. Compos. Mater. 9 (2019) 207–229, https://doi.org/10.4236/ojcm.2019.92012.
[7] S. Ahn, G. Kim, P.K. Nayak, S.I. Yoon, H. Lim, H. Shin, H.S. Shin, Prevention of transition metal dichalcogenide photodegradation by encapsulation with h-BN layers, ACS Nano 10 (2016) 8973–8979, https://doi.org/10.1021/acsnano.6b05042.
[8] N. Choudhary, M.A. Islam, J.H. Kim, T.J. Ko, A. Schropp, L. Hurtado, D. Weitzman, L. Zhai, Y. Jung Y, Two-Dimensional transition metal dichalcogenide hybrid materials for energy applications, Nano Today 19 (10) (2018) 1016, 1–80.
[9] R. Vargas-bernal, Graphene against Other Two-Dimensional Materials : A Comparative Study on the Basis of Photonic Applications World ' S Largest Science, Technology & Medicine Open Access book publisher, 2017, https://doi.org/10.5772/67807.
[10] W. Choi, I. Lahiri, R. Seelaboyina, Y.S. Kang, Synthesis of graphene and its applications: a review, Crit. Rev. Solid State Mater. Sci. 35 (2010) 52–71.
[11] T. Kuila, S. Bose, A. Kumar, P. Khanra, Progress in Materials Science Chemical Functionalization of Graphene and its Applications, vol. 57, 2012, pp. 1061–1105.
[12] K.S. Novoselov, A. Mischchenko, A. Carvalho, A. Castro Neto, 2D materials and van der Waals heterostructures, Science. AAAS 353 (2016), 0.1125/Science aac9439.
[13] A. Molina-sánchez, K. Hummer, L. Wirtz, Vibrational and optical properties of MoS_2 : from monolayer to bulk, Surf. Sci. Rep. 70 (2015) 554–586.
[14] N. Baig, Two-dimensional nanomaterials: a critical review of recent progress, properties, applications, and future directions, Compos. Appl. Sci. Manuf. 165 (2023) 107362, https://doi.org/10.1016/j.compositesa.2022.107362. ISSN 1359-835X.
[15] Z. Li, J. Chen, R. Dhall, S.B. Cronin, Highly efficient , high speed vertical photodiodes based on few-layer highly efficient , high speed vertical photodiodes based on few-layer MoS_2, 2D Mater. 4 (2017) 1–19.
[16] W. Wu, D. De, S. Chang, Y. Wang, H. Peng, J. Bao, S. Pei, et al., High mobility and high on/off ratio field-effect transistors based on chemical vapor deposited single-crystal MoS_2 grains, Appl. Phys. Lett. 102 (2013) 142106, https://doi.org/10.1063/1.4801861.
[17] N. Singh, G. Jabbour, U. Schwingenschl, Optical and photocatalytic properties of two-dimensional MoS_2, Eur. Phys. J. B 85 (10) (2012) 1140, https://doi.org/10.1140/epjb/e2012-30449-7, 2–5.
[18] B. Radisavljevic, A. Radenovic, J. Brivio, V. Giacometti, A. Kis, Single-layer MoS_2 transistors, Nat. Nanotechnol. 6 (3) (2011) 147–150, https://doi.org/10.1038/nnano.2010.279.
[19] W. Zhang, C.P. Chuu, J.K. Huang, C.H. Chen, M.L. Tsai, Y.H. Chang, C.T. Liang, Y.Z. Chen, Y.L. Chueh, J.H. He, M.Y. Chou, L.J. Li, Ultrahigh-gain photodetectors based on atomically thin graphene-MoS_2 heterostructures, Sci. Rep. 234 (2014) 3826.
[20] N.A. Kumar, M.A. Dar, R. Gul, J.-B. Baek, Graphene and molybdenum disulfide hybrids: synthesis and applications. Mater, Today Off. 18 (5) (2015) 286–298, https://doi.org/10.1016/j.mattod.2015.01.016.
[21] W. Fu, F.H. Du, J. Su, X.H. Li, X. Wei, T.N. Ye, K.X. Wang, J.S. Chen, In Situ catalytic growth of large-area multilayered graphene/MoS_2 heterostructures, Sci. Rep. 4 (2014) 4673.
[22] K. Murali, N. Abraham, S. Das, S. Kallatt, Highly sensitive , fast graphene photodetector with responsivity $> 10^6$ a/w using a floating quantum well gate, ACS Appl. Mater. Interfaces 11 (2019) 30010–30018.
[23] J. Yang, Y. Liu, H. Ci, F. Zhang, J. Yin, B. Guan, H. Peng, Z. Liu, High - performance 3D vertically oriented graphene photodetector using a floating indium tin oxide channel, Sensors 22 (3) (2022) 959, 10. 3390/s22030959.
[24] K. Roy, P. Medini, G.T. Srijit, C. Phanindra, R. Gopalakrishnan, R. Srinivasan, A. Ghosh, Graphene – MoS_2 hybrid structures for multifunctional photoresponsive memory devices, Nat. Nanotechnol. 8 (2013) 826–830, https://doi.org/10.1038/nnano.2013.206.
[25] J. Guo, L. Lin, S. Li, J. Chen, S. Wang, W. Wu, J. Cai, T. Zhou, Y. Liu, W. Huang, Ferroelectric superdomain controlled graphene plasmon for tunable mid-infrared photodetector with dual-band spectral selectivity, Carbon 189 (2022) 596–603.
[26] J. Guo, S. Li, L. Lin, J. Cai, J. Chen, S. Wang, X. Gou, J. Ye, Z. Luo, W. Huang, Enhanced-performance self-powered photodetector based on multi-layer MoS_2 sandwiched between two asymmetric graphene contacts, Sci. China Technol. Sci. 65 (11) (2022) 2658–2666.
[27] T. Hu, L. Zhao, Y. Wang, H. Lin, S. Xie, Y. Hu, C. Liu, W. Zhu, Z. Wei, J. Liu, K. Wang, High-sensitivity and fast-speed UV photodetectors based on asymmetric nanoporous-GaN/graphene vertical junction, ACS Nano 7 (9) (2023) 8411–8419.

[28] L. Kuo, V.K. Sangwan, S.V. Rangnekar, T.C. Chu, D. Lam, Z. Zhu, L. J Richter, R. Li, B. M Szydłowska, J. R Downing, B. J Luijten, All-Printed ultrahigh-responsivity MoS_2 nanosheet photodetectors enabled by megasonic exfoliation, Adv. Mater. 34 (34) (2022) 2203772.
[29] F.I. Alzakia, S.C. Tan, Liquid-exfoliated 2D materials for optoelectronic applications, Adv. Sci. 8 (11) (2021) 2003864.
[30] M.O. Awoji, A.D. Onoja, M.I. Echi, Synthesis of graphene via arc discharge and its characterization: a comparative approach, East European Journal of Physics 2 (1) (2023) 252–257. Mar.
[31] P.T. Gomathi, P. Sahatiya, S. Badhulika, Large-Area, flexible broadband photodetector based on ZnS–MoS_2 hybrid on paper substrate, Adv. Funct. Mater. 27 (2017) 1701611.
[32] P. Sahatiya, S. Badhulika, Strain-modulation-assisted enhanced broadband photodetector based on large-area, flexible, few-layered Gr/MoS_2 on cellulose paper, Nanotechnology 28 (45) (2017) 455204.
[33] D. De Fazio, et al., High responsivity, large-area graphene/MoS_2 flexible photodetectors, ACS Nano 10 (2016) 8252–8262, https://doi.org/10.1021/acsnano.6b05109.
[34] V.D. Paolucci, G. Olimpio, L. Lozzi, A.M. Mio, L. Ottaviano, M. Nardone, G. Nicotra, P. Le-Cornec, C. Cantalini, A. Politano, Sustainable liquid-phase exfoliation of layered materials with nontoxic polarclean solvent, ACS Sustain. Chem. Eng. 8 (51) (2020) 18830–18840, https://doi.org/10.1021/acssuschemeng.0c04191.
[35] Y. Xu, H. Cao, Y. Xue, B. Li, W. Cai, Liquid-phase exfoliation of graphene : an overview on exfoliation media , techniques, and challenges, Nanomaterials 8 (11) (2018) 942, https://doi.org/10.3390/nano8110942.
[36] J. Kim, et al., Materials in Pure Water via Temperature Control, 2015, https://doi.org/10.1038/ncomms9294.
[37] P.M. Biranje, A.W. Patwardhan, J.B. Joshi, K. Dasgupta, Exfoliated graphene and its derivatives from liquid phase and their role in performance enhancement of epoxy matrix composite, Compos. Part A 156 (2022) 106886.
[38] W. Choi, I. Lahiri, R. Seelaboyina, Y.S. Kang, Synthesis of graphene and its applications: a review, Crit. Rev. Solid State Mater. Sci. 8436 35 (2010) 52–71.
[39] S.S. Shams, R. Zhang, J. Zhu, Graphene synthesis : a review, Mater. Sci. (2015), https://doi.org/10.1515/msp-2015-0079.
[40] A.K. Geim, P. Kim, Carbon Wonderland, Scientific American, 2008, pp. 90–98.
[41] H. Tian, M.L. Chin, S. Najmaei, Q. Guo, F. Xia, H. Wang, M. Dubey, Optoelectronic devices based on two-dimensional transition metal dichalcogenides, Nano Res. 9 (6) (2016) 1543–1560, https://doi.org/10.1007/s12274-016-1034-99.
[42] M. Hashemi, N. Ansari, M. Vazayefi, MoS_2 - based absorbers with whole visible spectrum coverage and high efficiency, Sci. Rep. (2022) 1–9, https://doi.org/10.1038/s41598-022-10280-2.
[43] S. Rathi, I. Lee, D. Lim, J. Wang, Y. Ochiai, N. Aoki, K. Watanabe, T. Taniguchi, G.H. Lee, Y.J. Yu, Tunable electrical and optical characteristics in monolayer graphene and few-layer MoS_2 heterostructure devices, Nano Lett. 15 (2015) 5017–5024.
[44] Y. Zhang, J. Shi, M. Liu, J. Wen, X. Ren, X. Zhou, Q. Ji, D. Ma, Y. Zhang, C. Jin, All chemical vapor deposition synthesis and intrinsic bandgap observation of MoS_2/Graphene heterostructures, Adv. Mater. 27 (2015) 7086–7092.
[45] A. Pandey, A. Mukherjee, S. Chakrabarty, D. Chanda, S. Basu, Interface engineering of an RGO/MoS_2/Pd 2D heterostructure for electrocatalytic overall water splitting in alkaline medium, ACS Appl. Mater. Interfaces 11 (2019) 42094–42103.
[46] Y. Kim, D. Choi, W.J. Woo, J.B. Lee, G.H. Ryu, J.H. Lim, S. Lee, Z. Lee, S. Im, J.H. Ahn, Synthesis of two dimensional MoS_2/Grapheneheterostructure by atomic layer deposition using MoF precursor, Appl. Surf. Sci. 494 (2019) 591–599.
[47] K.S. Novoselov, V.I. Fal ko, L. Colombo, P.R. Gellert, M.G. Schwab, K. Kim, A roadmap for graphene, Nature 490 (2012) 192–200.
[48] Q. Qiu, Z. Huang, Photodetectors of 2D materials from ultraviolet to terahertz waves, Adv. Mater. 33 (2021) 1–19, 2008126.
[49] A.D. Yoffe, Low-dimensional systems: quantum size effects and electronic properties of semiconductor microcrystallites (zerodimensional systems) and some quasi-two-dimensional systems, Adv. Phys. 51 (2) (2002) 799–890.
[50] A. Castellanos-gomez, J. Quereda, H.P. Meulen, N. Agraït, G. Rubio-Bollinger, Spatially resolved optical absorption spectroscopy of single- and few-layer MoS_2 by hyperspectral imaging, Nanotechnology 27 (2016) 115705. http://iopscience.iop.org/0957-4484/27/11/115705.
[51] D. Sangalli, K. Hummer, A. Marini, L. Wirtz, Effect of spin-orbit interaction on the optical spectra of single-layer, double- layer, and bulk MoS_2, Phys. Rev. B (2013), https://doi.org/10.1103/PhysRevB.88.045412.
[52] B. Visic, R. Dominko, M.K. Gunde, N. Hauptman, S. D Skapin, M. Remskar, Optical properties of exfoliated MoS_2 coaxial nanotubes - analogues of graphene, Nanoscale Res. Lett. 6 (2011) 593. http://www.nanoscalereslett.com/content/6/1/5931–6.
[53] H. Kaur, J.N. Coleman, Liquid-phase exfoliation of nonlayered non-van-der-waals crystals into nanoplatelets, Adv. Mater. 34 (2022), https://doi.org/10.1002/adma.202202164, 2202164 1-220216420.
[54] D.M. Kandhasamy, P.M. Mareeswaran, S. Chellappan, D. Namasivayam, A. Aldahish, K. Chidambaram, Synthesis and photoluminescence properties of MoS_2/Graphene heterostructure by liquid-phase exfoliation, ACS Omega 7 (2022) 629–637, https://doi.org/10.1021/acsomega.1c05250.
[55] A.R. Klots, A.K.M. Newaz, B. Wang, D. Prasai, H. Krzyzanowska, J. Lin, D. Caudel, N.J. Ghimire, J. Yan, B.L. Ivanov, K.A. Velizhanin, A. Burger, D.G. Mandrus, N.H. Tolk, S.T. Pantelides, K.I. Bolotin, Probing excitonic states in suspended two-dimensional semiconductors by photocurrent spectroscopy, Sci. Rep. 4 (2014) 6608, https://doi.org/10.1038/srep06608, 1–7|.
[56] R.J. Smith, P.J. King, M. Lotya, C. Wirtz, U. Khan, S. De, A. O'Neill, G.S. Duesberg, J.C. Grunlan, G. Moriarty, J. Chen, J. Wang, A.I. Minett, Valeria Nicolosi, J. N. Coleman, Large-Scale exfoliation of inorganic layered compounds in aqueous surfactant solutions, Adv. Mater. 23 (2011) 3944–3948, https://doi.org/10.1002/adma.201102584.
[57] P.R. Jubu, F.K. Yam, Developmennt and characterization of MSM UV photodetector based on gallium oxide nanostructures, Sensor. Actuator. 312 (2020) 112141.
[58] P.R. Jubu, O.S. Obaseki, F.K. Yam, S.M. Stephen, A.A. Avaa, A.A. McAsule, Y. Yusof, D.A. Otor, Influence of the secondary absorption and the vertical axis scale of the Tauc's plot on optical bandgap energy, J. Opt. 52 (3) (2023) 1426–1435. Sep.
[59] P.R. Jubu, O.S. Obaseki, A.N. Abutu, F.K. Yam, Y. Yusof, M.B. Ochang, Dispensability of the conventional Tauc's plot for accurate bandgap determination from UV–vis optical diffuse reflectance data, Results in Optics 9 (2022) 100273, https://doi.org/10.1016/j.rio.2022.100273. ISSN 2666-9501.
[60] M.B. Ochang, I. Ahemen, A.N. Amah, P. R Jubu, A.D. Onoja, D.D. Hile, Y. Yusof, Influence of Mn content on the optical, structural and electrical properties of spray pyrolysis deposited quinternary Cu_2Cd1- x MnxSnS4 thin films for solar cells, Opt. Quant. Electron. 55 (6) (2023) 560.
[61] G.A. M Ali, M.R. Thalji, W. C Soh, H. Algarni K.F. Chong, One step electrochemical synthesis of MoS_2/Graphene composite for supercapacitor application, J. Solid State Electrochem. (2019), https://doi.org/10.1007/S10008-019-04449-5.
[62] S.K. Chakraborty, B. Kundu, B. Nayak, S.P. Dash, Challenges and opportunities in 2D heterostructures for electronic and optoelectronic devices, iScience 25 (2022) 103942.
[63] M. L Hegde, T.K. Hazra, S. Mitra, Early Steps in the DNA Base Excision/Single-Strand Inter- Ruption Repair Pathway in Mammalian Cells, vol. 1, 2008, pp. 27–47.
[64] Y. Zhang, R. Liu, On Valence-Band Splitting in Layered, 2015, https://doi.org/10.1021/acsnano.5b03505.
[65] C. Backes, R.J. Smith, N. Mc-Evoy, N.C. Berner, D. McCloskey, H.C. Nerl, A. O'Neill, P.J. King, T. Higgins, D. Hanlon, Edge and confinementeffects allow in situ measurement of size and thickness of liquid exfoliated nanosheets, Nat. Commun. 5 (2014) 4576.
[66] S.S. Sarkar, S. Mukherjee, R.K. Khatri, S.K. Ray, Solution processed MoS_2 quantum dots/GaAsvVertical heterostructures based self-powered photodetectors with superior detectivityt, Nanotechnology (2019), https://doi.org/10.1088/1361-6528/ab5f05 s.
[67] P.M. Pataniya, C.K. Sumesh, WS_2 nanosheet/graphene heterostructures for paper-based flexible photodetectors, ACS Appl. Nano Mater. 10 (2020) 1021, https://doi.org/10.1021/acsanm.0c01276.
[68] M.V. Bracamonte, G.I. Lacconi, S.E. Urreta, L. E Torres, On the nature of defects in liquid-phase exfoliated graphene, J. Phys. Chem. C 10 (2014) 1021, https://doi.org/10.1021/jp501930a.
[69] C. Chen, H. Qiao, S. Lin, et al., Highly responsive MoS_2 photodetectors enhanced by graphene quantum dots, Sci. Rep. 5 (2015) 11830, https://doi.org/10.1038/srep11830.

[70] W. Zhang, C.P. Chuu, J.K. Huang, C. H Chen, M.L. Tsai, Y.H. Chang, C.T. Liang, Y.Z. Chen, Y.L. Chueh, J.H. He, M.Y. Chou, L.J. Li, Ultrahigh-gain photodetectors based on atomically thin graphene-MoS_2 heterostructures, Sci. Rep. J4 (2014) 3826, https://doi.org/10.1038/srep03826. PMID: 24451916; PMCID: PMC3899643.
[71] P.V. Pham, S.C. Bodepudi, K. Shehzad, Y. Liu, Y. Xu, B. Yu, X. Duan, Chem. Rev. 122 (6) (2022) 6514–6613DOI, https://doi.org/10.1021/acs.chemrev.1c00735.
[72] B. Liu, Y. Chen, C. You, Y. Liu, X. Kong, J. Li, S. Li, W. Deng, Y. Li, H. Yan, Y. Zhang, High performance photodetector based on graphene/MoS_2/graphene lateral heterostrurcture with Schottky junctions, J. Alloys Compd. 779 (2019) 140–146, https://doi.org/10.1016/j.jallcom.2018.11.165. ISSN 0925-8388.
[73] P. Vabbina, N. Choudhary, A. Chowdhury, R. Sinha, M. Karabiyik, S. Das, W. Choi, N. Pala, Highly sensitive wide bandwidth photodetector based on internal photoemission in CVD grown p-type MoS_2/Graphene Schottky junction, ACS Appl. Mater. Interfaces 7 (28) (2015) 15206–15213, https://doi.org/10.1021/acsami.5b00887.
[74] S. Ghosh, A. Winchester, B. Muchharla, M. Wasala, S. Feng, A.L. Elias, M.B.M. Krishna, T. Harada, C. Chin, K. Dani, S. Kar, M. Terrones, S. Talapatra, Ultrafast Intrinsic photoresponse and direct evidence of sub-gap states in liquid phase exfoliated MoS_2 thin films, Sci. Rep. 5 (2015) 11272, https://doi.org/10.1038/srep11272.